Semi-Empirical Model for the Prediction of Surface Vibration Amplitudes of Kilowatt Class Electric Motors

Jordan D. Cluts[1], Brenda S. Henderson[2], Gregory R. Busch[3]
NASA Glenn Research Center, Cleveland, OH, 44135, U.S.A.

The ongoing integration of outrunner brushless electric motors into drones and Urban Air Mobility aircraft presents a need for electric motor acoustic predictions suitable for system-level studies. A motor-noise prediction model allows motor acoustics to be incorporated into early vehicle design trade studies. An ongoing effort to develop a motor-noise prediction model, for integration into other system-level tools, is underway. The model is comprised of three main elements which predict the electromagnetic forcing, the induced structural vibrations, and the resulting acoustic propagation. This work discusses the structural vibration element and describes a method to predict surface vibration amplitudes of the motor rotor. The surface displacement amplitude is a requirement for the acoustic propagation element. To accurately predict the rotor displacement, accurate damping values for the rotor structure are required. An experimental investigation of damping values for 1-5kW class motors are presented. A parametric sweep and least-squares-curve fit to a finite element analysis yields a simple curve that can predict vibration amplitude based on a particular driving frequency and mode shape.

I. Introduction

Brushless DC electric motors are commonly used on small unmanned aerial systems (sUAS) and larger urban-air-mobility (UAM) electric aircraft. These motors are often directly coupled to a vehicle's propellors/rotors and are unlikely to have a weighty enclosure to significantly attenuate noise. Noise generated by the motor can directly add to the overall vehicle noise signature [1,2]. A low-fidelity tool, suitable for implementation in system-type studies to assist in the early design phases of future electric air vehicles is needed. Such a tool would allow motor acoustics to be accurately considered in the conceptual-design trade space. A critical element of such a tool is the accurate prediction of motor surface vibration amplitudes. This paper develops a semi-empirical model that estimates the vibration amplitude required for the acoustic radiation model used to predict electric motor noise.

In this work, we focus our attention on brushless DC outrunner radial flux electric motors where the stator is in the motor interior and the motor rotor (here after referred to simply as the rotor) is on the exterior of the motor. Most often, the propulsor is directly coupled to this rotor, although configurations with a gear reduction are possible.

Electric motor noise is composed of a number of sources, including those generated by the vibration of the motor outer structure, the bearings, the noise of electric components, and the aerodynamic noise caused by rotating components disturbing the air around them [3]. Among these, structural vibrations generate noise by the displacement of the rotor outer surface [4,5]. Structural vibrations are driven by the fluctuating magnetic field imparting a force on the stator and rotor. In outrunner motors, the forcing on the rotor generates radial surface displacements with sufficient surface velocities to emit acoustic radiation. This three-step process [6-9] of noise generation is depicted in Fig. 1.

[1] AIAA Member
[2] AIAA Associate Fellow
[3] AIAA Member

Each of the three elements in this process must be adequately modeled to predict sound. The induced vibrations of the rotor structure of outrunner motors are investigated in this effort. Structural vibrations can also generate noise via transfer of the vibration to the motor mounting structure, but that is beyond the scope of the current effort.

An ongoing effort is underway to create a tool suitable for high-level design and analysis to predict each of the three elements of the noise generation model. The implementations of these three elements are referred to as the electromagnetic forcing model, the structural vibration model, and the acoustic propagation model. When combined, they will allow for an acoustic prediction derived from high-level motor parameters and operating conditions. The electromagnetic forcing model generates a prediction of the forcing applied to the rotor. The mode shape, amplitude, and frequency of this forcing becomes the input to the structural vibration model which predicts the resulting rotor surface vibrations. Lastly, the surface vibration modes, frequency, and amplitudes are used by the acoustic propagation model to predict the resulting acoustic radiation.

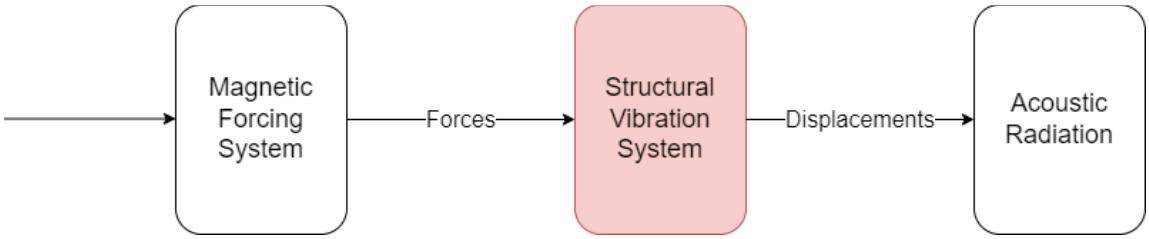


Fig. 1 Three step motor acoustic prediction model derived from Ref. [11].

A completed model comprised of these three elements could be used in modeling vehicles for noise impact assessments or altering vehicle motor design to avoid motor resonance modes. Vehicle control law is another avenue to mitigate noise with the data provided by a completed model. If it is known that a resonance will occur under specific conditions for a given configuration, a vehicle control law can be configured to avoid those regimes.

In a previous work [10], a semi-empirical model was built to predict eigenmodes and eigenfrequencies of outrunning electric motor rotors in the 1-5 kW class. A finite-element analysis (FEA) simulation was used to distill a semi-empirical curve fit that predicted eigenmode shapes and eigenfrequencies using a limited set of motor geometric parameters. Using the semi-empirical model is computationally inexpensive and it requires limited details about a motor, allowing predictions during the conceptual design phase. This previous element represents one part of the structural vibration model. The current work presents an update of the structural vibration model to predict the amplitude of the rotor vibrations driven by electromagnetic forcing.

An FEA distillation in a manner similar to the previous [10] is performed. Forcing of the rotor structure, analogous to those imposed by the stator, are added to the simulation. This forcing is characterized by azimuthal mode shape and frequency. The simulations generate normalized rotor displacement data that is required to predict vibration amplitudes in the completed tool. These simulations are performed over a geometric space of relevance for motors of the class and type investigated. These geometries are defined using the parameterized rotor geometry developed previously [10]. The rotor diameter and aspect ratio are varied to explore their impact on rotor structural vibrations.

The previous eigenmode and eigenfrequency prediction component did not require structural damping to be modeled. For the amplitude predictions, damping cannot be neglected to accurately predict the structural displacement caused by vibrations near resonance. An experimental investigation of damping values for two motors are presented as well as comparisons of the observed resonance frequencies with acoustic measurements.

This work describes the addition of forced vibrations into an FEA simulation in Section II A. Section II B discusses experimental damping coefficient measurements needed by that FEA simulation. Next, acoustic measurements are described which serve to contextualize the vibration frequencies measured during the damping coefficient measurements. The results of the damping experiments follow in Section III B. Then, the results of the simulations across a range of rotor geometries are presented in Section III C and D. This includes normalization and curve fits of the simulations' results and a description of their use to generate a prediction.

II. Methodology

A. COMSOL Simulations

In order to build upon the previous eigenfrequency prediction tool, radial forcing on the rotor surface was added to the COMSOL Multiphysics FEA simulation. This forcing, depicted in Fig. 2, has three parameters, azimuthal mode number, frequency, and amplitude. The azimuthal mode number corresponds to the eigenmode shape that was

identified in the previous eigenmode analysis. These eigenmode shapes are analogized to vibrational modes in a finite ideal cylinder. For such a cylinder, a given vibration mode is fully characterized by an azimuthal mode number and an axial mode number, *m* and *n*, respectively. A given rotor eigenmode can be identified by the *m* and *n* mode numbers that correspond with the displacement of the rotor surface. Examined motors exhibit predominantly $n = 1$ axial mode shapes including all modes discussed herein, consequently only the azimuthal mode number, *m*, will be specified. The forcing applied to the rotor in the simulation is also described by the azimuthal mode number. Rotor forcing with a given azimuthal mode number will excite rotor eigenmodes that match that mode number. As a result, excitation using each mode number is required.

The geometry used in the FEA simulation is a parameterized model representative of many rotors in the 1-5kW class of electric motors. It is a simplified rotor geometry characterized by ten parameters: rotor diameter, rotor height, spoke thickness, rotor wall thickness, magnet width, magnet thickness, number of magnets, number of spokes, rotor flange width, and shaft diameter. Among five motors investigated, diameter and aspect ratio vary considerably. As a result, these parameters were selected for investigation. Details of the geometry and its development are provided in Ref. [8]. For convenience, the height of the simulated motor geometry is non-dimensionalized to aspect ratio (diameter/height) which better preserves realistic rotor geometries as motor diameter changes. Diameter is varied from 20-100mm and aspect ratios from 0.7-7.0. In total, 63 different parameter combinations are simulated within the geometry space. The range of rotor geometries is depicted in Fig. 3.

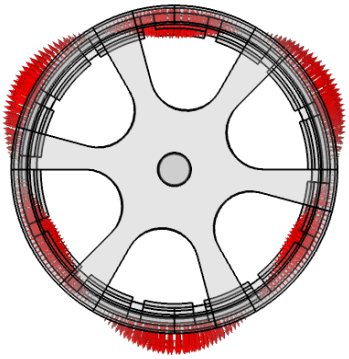


Fig. 2 Azimuthal mode *m* = 3 radial forcing applied to the surface of the parameterized motor geometry.

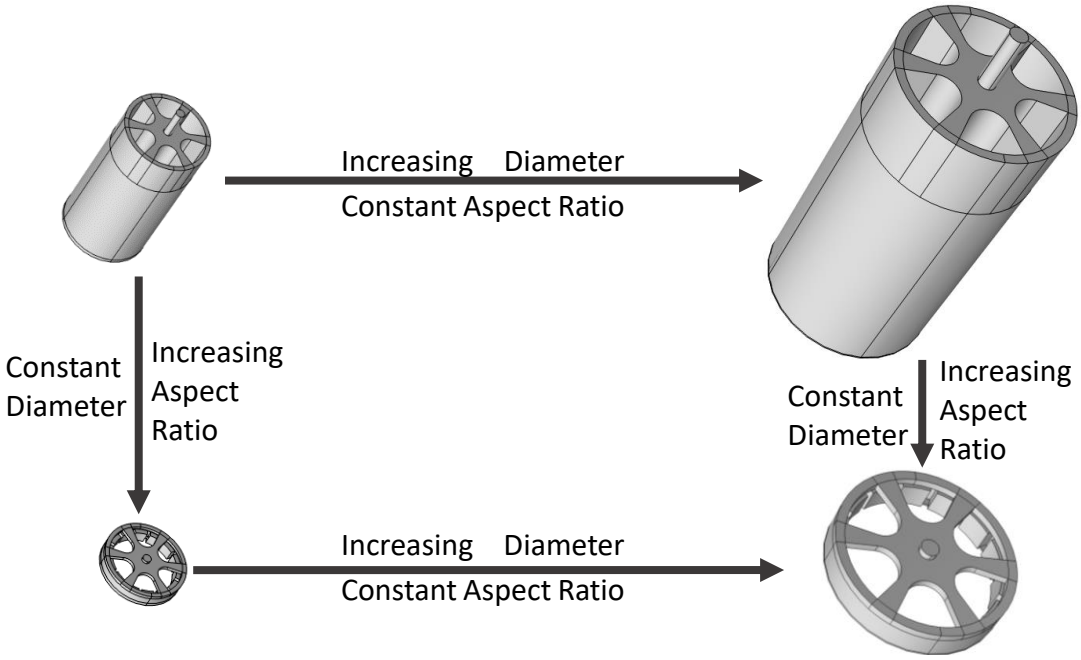


Fig. 3 Illustration of geometric parameter space explored with varying rotor diameter and aspect ratio.

The frequency of the forcing applied to the rotor will impact the amplitude of the resulting vibration via its proximity to the eigenfrequency or frequencies of the eigenmode(s) that correspond to the forcing mode number. Previous studies [12] have indicated that a typical, acoustically relevant, surface vibration may be caused by surface displacement amplitudes in the 5-100 μm range. While the displacement is small, the surface velocity can be large leading to a large amplitude in the resulting acoustic tones. Due to the small displacement magnitude, it is assumed that the displacement is linear with the forcing amplitude. For the simulations, 1 N/m^2 is used as the forcing amplitude. Due to the linear relationship, the final predicted surface displacement for a given motor can be found by multiplying the predicted value of the simulation by the applied electromagnetic forcing amplitude.

In the previous work, damping was not required to predict eigenvalues and eigenfrequencies. In this effort, where the objective is absolute displacement magnitude, it must be included. Without damping, forced vibration of the simple rotor structure leads to singularities when the forcing frequency matches the corresponding eigenfrequency. COMSOL Multiphysics automatically handles the implementation of damping and can use several different models. The simplest of these models is *isotropic loss factor* which creates a single defined decay rate for all frequencies. For this model, however, knowledge of this loss factor is required. A priori this is difficult to determine without experimental data.

A more sophisticated model is the *Rayleigh damping model*. This is a two-parameter model which uses measured damping coefficients at two non-harmonically related frequencies to predict damping values across all frequencies for a given structure. This model requires detailed knowledge about the test article and the requisite frequency/damping value pairs are commonly measured empirically. Here, the damping values are determined experimentally.

Another detail that must be accounted for is the relevant material properties. This is challenging to parameterize. An inspection of several motors in this class has indicated that the spoke structure is typically comprised of aluminum, while the cylindrical rotor body is steel or aluminum. The magnets are assumed to be N52 ceramic and the motor shaft is hardened steel. For more details on material properties used in the model, see [10]. For this work, the rotor spokes and body are modeled as aluminum, with N52 ceramic magnets and hardened-steel shaft, a set of materials which match the structure of the motors investigated.

B. Experimental Motor Structural Damping Coefficient Measurement

Damping coefficients were determined for a Scorpion SII 4020 and a T-Motor U13. Each motor was suspended by the spokes with fishing line to create a free vibration condition. Each rotor was instrumented with one PCB Piezotronics model 352C23 accelerometer. Beeswax was used to adhere the accelerometer to the rotor cylindrical surface, oriented to measure acceleration in the radial direction. The accelerometer was placed near the bottom of the rotor (furthest from the spokes) where FEA eigenmode analysis indicated the largest radial displacements typically occur. A PCB Piezotronics modal impact hammer, model 086E80 utilizing the model 084A14 handle, was used to excite the resonant modes of the rotor. Neither the optional rubber tip nor extender mass supplied with the modal impact hammer to decrease the excitation frequency were employed. The modal impact hammer was used to strike the rotor perpendicular to the main cylindrical rotor surface. The hammer strikes were aimed more than 90 degrees away from the accelerometer position on the rotor.

Data from both the accelerometer and the modal impact hammer were acquired using a National Instruments PXIe 4499 Sound and Vibration card at 200,000 samples/s. Records with double strikes, misses, etc. were removed from the final analysis. Accepted recordings typically exhibited a strike followed by at least 0.1 s of clean vibration decay recorded by the data acquisition system.

For each accelerometer time history, spectral peaks were identified, and a corresponding bandpass filter was applied. An example of the bandpass-filtered time history is depicted in Fig. 4. A simple heuristic was applied to locate a segment of the bandpass-filtered time history for which the vibration amplitudes were decaying. The peak of each oscillation period defines the vibration decay envelope. An exponential curve with amplitude, *A*, and decay rate, λ, of the form in Eq. 1 was fit to this envelope. The fit region and an example fit are also shown in Fig. 4. The damping ratio, ζ can be calculated from the angular frequency, ω, and the decay rate as shown in Eq. 2.

$$Volts = Ae^{-\lambda t} \tag{1}$$

$$\zeta = \frac{\lambda}{\sqrt{\lambda^2+\omega^2}} \tag{2}$$

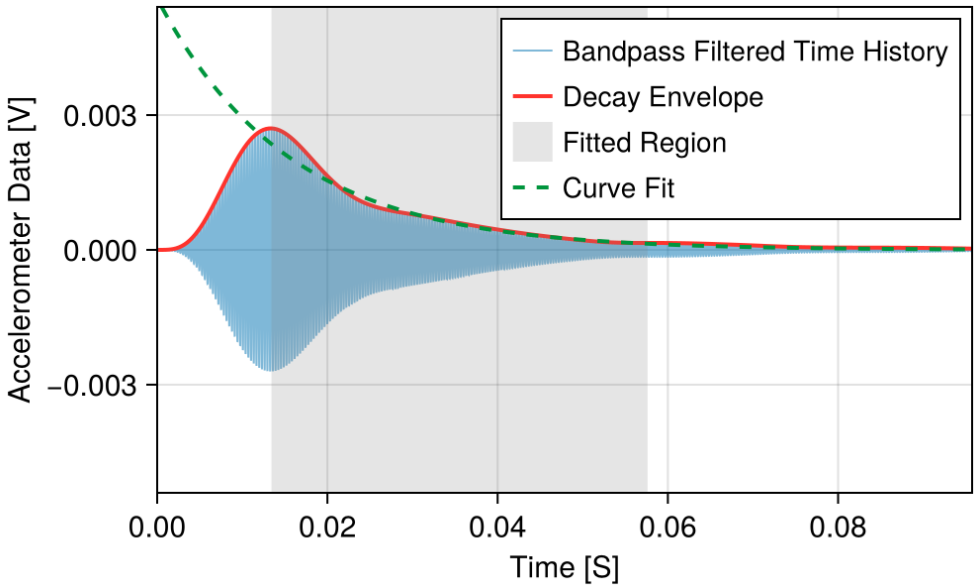


Fig. 4 Scorpion SII 4020 vibration decay curve fit, filtered around 3143 Hz.

C. Acoustic Measurement Methodology

Acoustic measurements were conducted in the anechoic chamber of the Acoustic Testing Laboratory (ATL) at the NASA Glenn Research Center (see Fig. 5). The interior dimensions of the chamber are 6.4 m deep x 5.2 m wide x 5.2 m high. The floor consists of removable steel grating panels suspended over wedges. The steel gratings remained in place for the experiments. The chamber cut-off frequency is 100 Hz. The motors were suspended near the center of the chamber with nylon fishing line as shown in Fig. 6 (a). The fishing line limited unwanted vibrations and associated sound generation that occurs when mounting a motor on a sting. A T-Motor FLAME Series Electronic Speed Controller was used with an external pulse-width modulation signal to control the motor speed.

The acoustic measurements were made with ¼" 46BE GRAS free-field microphones mounted in the configuration shown in Fig. 6 (b). The distance from the indicated center points to the microphones was 1 m. The microphones were calibrated for sensitivity prior to the test. The data were acquired with an NI 4499 PXIe card at a sampling rate of 100,000 samples/s. Sound pressure level (SPL) spectra were obtained with a 16384-point FFT using a Hamming window and 50% overlap. The resulting binwidth was 6.1035 Hz. A tachometer signal, recorded simultaneously with the acoustic signals, was used to compute motor speed.

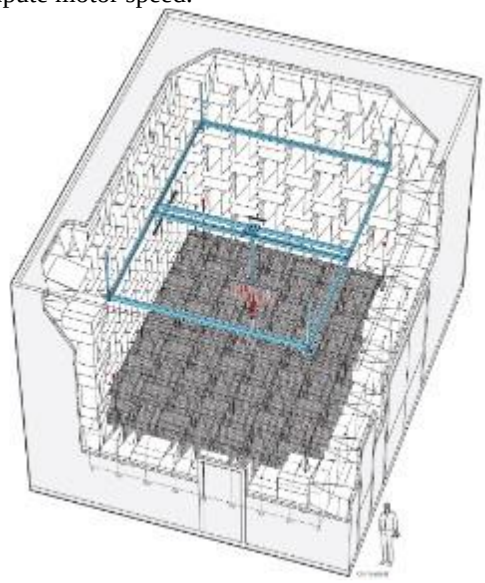


Fig. 5 A schematic of the Acoustic Test Laboratory (ATL) at the NASA Glenn Research Center.

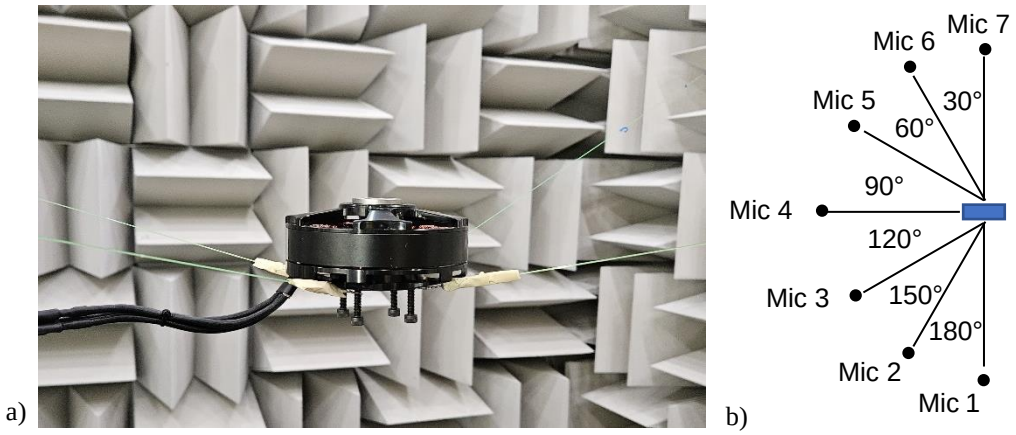


Fig. 6 (a) U13 motor mounted in the ATL. (b) Microphone array used in the electric motor noise experiments.

III. Results

A. Acoustics

Acoustic measurements provide data about tones generated by motors during operation. The frequencies and corresponding azimuthal modes of observed acoustic tones serve to focus tool development on modes of interest. The acoustic radiation at microphone 4 for the Scorpion motor is shown in Fig. 7. The data were acquired at a motor speed of 6292 rpm. Also shown in the Figure are the harmonics of the electrical line frequency. The peak radiation occurs near 3000 Hz at the fourth electrical harmonic. The tone occurs at a frequency close to that found for the second azimuthal mode in the previous FEA eigenmode analysis. The tone at roughly 3400 Hz is also likely associated with the second azimuthal mode as its frequency is greater than that of the 3000 Hz tone by four times the motor speed. Azimuthal modes of a rotating cylinder propagate in the forward (with the cylinder rotation) and backward (opposite the cylinder rotation) directions in a stationary frame at propagation speeds equal to the mode number multiplied by the motor speed which, for mode two, results in a frequency difference between the forward and backward modes of four times the motor speed. It should be noted that the previous and current FEA analyses do not account for rotation of the vibration modes. Also observed in the spectra is a significant tone near 7300 Hz at the tenth electrical harmonic frequency. This tone is close to the frequency found previously for the fourth azimuthal vibration mode. The results of the acoustic measurements indicate that the second and fourth vibration modes are of interest in the vibration model used to predict motor tones for the Scorpion motor.

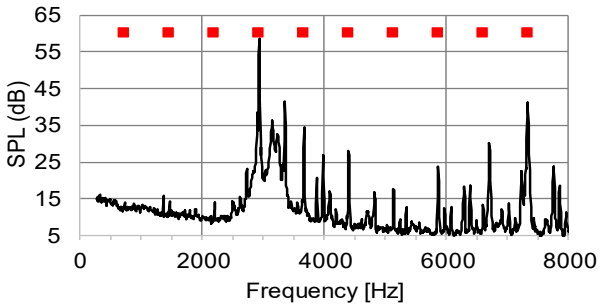


Fig. 7 The acoustic spectra acquired at microphone 4 for the Scorpion motor operating at 6292 rpm. The red squares indicate the harmonics of the electrical line frequency.

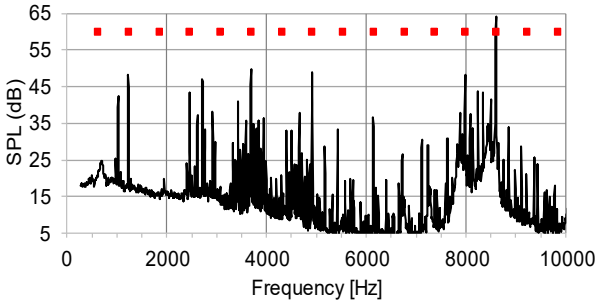


Fig. 8 The acoustic spectra acquired at microphone 4 for the U13 motor operating at 6071 rpm. The red squares indicate the harmonics of the electrical line frequency.

The acoustic spectrum for the U13 motor is shown in Fig. 8. More tones are observed for the U13 than for the Scorpion and, therefore, the number of modes included in the general vibration model will need to be expanded beyond modes two and four. The peak tone occurs at roughly 8600 Hz which is close to the frequency for mode six found in the previous FEA eigenmode analysis. The tone near 8000 Hz is also likely associated with mode six as the 8600 Hz

and 8000 Hz tones represent a forward and backward propagating pair. The two tones near 1000 Hz represent a tone pair for mode two. Some of the tones near 2700 Hz have frequencies near that expected for mode one. Finally, some of the tones between 4600 Hz and 4900 Hz are likely associated with a mode related to mode two. A discussion of mode identification and about multiple modes with the same mode number coexisting follows in Section III B. The results of the acoustic analysis for the U13 motor indicate the vibration model needs to predict modes up to $m = 6$ for accurate acoustic predictions.

B. Experimental Damping Coefficients

Damping coefficients are extracted from several vibration time histories as described in Section II B. Each band-pass-filtered time history, of which there can be several, from a single accepted strike is processed. The resulting damping coefficients for each mode and the corresponding vibration frequency, are depicted in Fig. 9 (a) and (b) for the Scorpion and U13 motors. The stator was not installed for the collection of this data. For the Scorpion, the measured coefficients are clustered into three clear groups near 1250 Hz, 3125 Hz, and 7275 Hz. In Fig. 9 (b) there are more groupings due to the larger number of eigenmodes present in the U13 motor as a consequence of the larger diameter and higher aspect ratio.

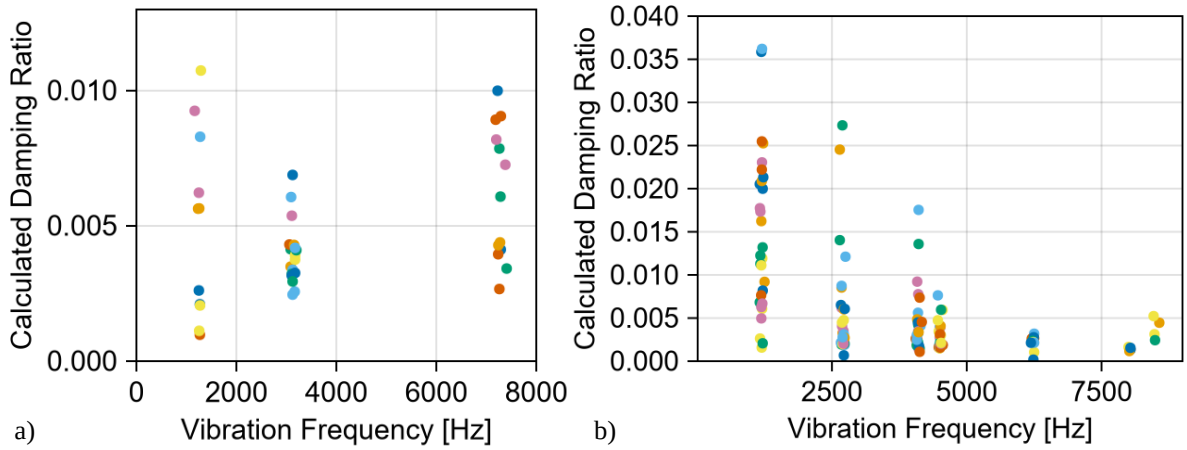


Fig. 9 Measured vibration damping coefficients vs vibration frequency with no stator for the a) Scorpion SII 4020 and b) U13 motors.

Table 1 shows data derived from Fig. 9 (a) and (b). For each cluster of data in Fig. 9, the mean frequency, mean damping coefficient, and the standard deviation of the damping coefficient have been calculated. In addition, the mode shape identified by the previous eigenmode analysis is also provided.

For the U13 rotor there are two different resonant frequencies, 1197 Hz and 4507 Hz that are labeled 2a and 2b respectively. Ordinarily a particular eigenmode can only be associated with one resonant frequency. For these rotors, the azimuthal mode numbers are analogous to those in idealized cylinders. In the case of these two modes, however, that analogy slightly breaks down. While each of these two modes are, when viewed through the narrow lens of surface mode shape, most similar to the $m = 2$ mode in an ideal cylinder, they both are in reality three-dimensional vibration modes and are distinct in ways that are not captured by the simple azimuthal mode number description. For more details on azimuthal mode shape categorization in motor rotors, see Ref [10].

Fig. 10 shows data for the U13 motor with the stator. The first four data groupings are recognizable as similar to the first four without the stator (Fig. 9 (b)), however, each has shifted to a slightly higher frequency indicating that the presence of the stator likely stiffens the rotor structure. Above 5 kHz, what previously was three groupings ranging from 6-9 kHz has been reduced to two.

Table 1 Damping coefficient of vibration frequency groups for Scorpion and U13 motors without stators.

Motor	Corresponding Mode Shape	Mean Frequency [Hz]	Mean Damping Coefficient	Standard Deviation of Damping Coefficient
Scorpion	1	1254	0.004970	0.003439
Scorpion	2	3132	0.003934	0.001139
Scorpion	4	7273	0.006171	0.002489
U13	2a	1197	0.016779	0.014961
U13	1	2705	0.004294	0.003245
U13	3	4099	0.004427	0.003838
U13	2b	4507	0.003106	0.001669
U13	4	6230	0.002209	0.000825
U13	5	8025	0.001416	0.000185
U13	6	8503	0.003809	0.001263

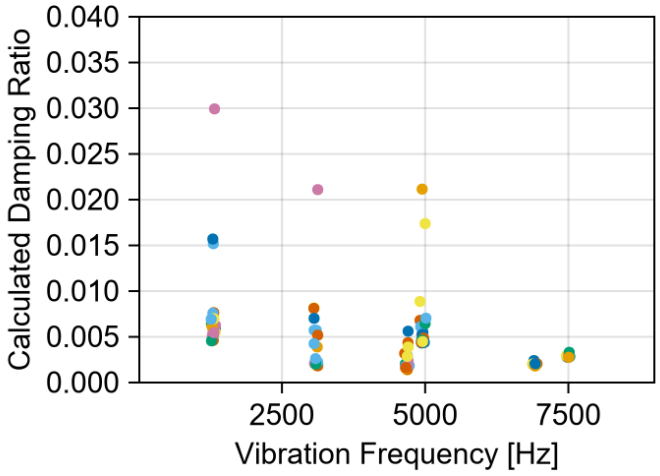


Fig. 10 Vibration damping coefficients vs vibration frequency for U13 motor with stator.

Table 2 shows the mean values for the first four clusters of damping values for the U13 motor with stator. The higher frequency clusters are omitted because their correspondence to the groups in the no-stator case are unknown and the identification of their mode shape via eigenmode analysis is less clear. For the first four modes however, the resulting damping coefficients fall into a similar range of values as the no-stator case. Across the four modes there is no clear directionality to the change in measured damping value from the no-stator case to the stator-present case with the data showing a mix of increases and decreases. The lowest frequency mode has the largest change. In the no-stator case, that grouping had a damping value, 0.016779, that is significantly higher than any other measured modes. In contrast, when the stator is installed, the damping value falls to just 0.005859, close to the values for the other modes investigated.

Table 2 Damping coefficient of vibration frequency groups for U13 motor with stator.

Motor	Corresponding Mode Shape	Mean Frequency [Hz]	Mean Damping Coefficient	Standard Deviation of Damping Coefficient
U13	2a	1301	0.005859	0.000906
U13	1	3091	0.003931	0.002289
U13	3	4683	0.002398	0.001117
U13	2b	4951	0.005388	0.001275

C. Frequency Response Curve

The amplitude displacement prediction generated by a sweep of the forcing frequency space around a given eigenmode and eigenfrequency is depicted in Fig. 11. The frequency sweep for this, and other simulations, is performed at 20 Hz intervals. The figure shows the surface displacement amplitude per unit of applied forcing pressure for a particular forcing mode shape, in this case $m = 2$. The surface displacement amplitude is the maximum absolute radial displacement, relative to the neutral position, achieved at any point on the outer rotor surface in the simulation. This value describes the most dynamic point on the rotor surface which is also the most relevant for acoustic radiation. The resonance amplitude is also indicated on Fig. 11. The resonance point is the maximum displacement on the response curve. The two curves correspond to the two different damping models available within COMSOL Multiphysics. For this simulation the isotropic loss factor is 0.008. The Rayleigh model used the Scorpion motor damping coefficients at 3132 Hz and 7273 Hz from Table 1. The user is only required to supply these four values (frequencies and corresponding damping values). The geometry and damping coefficients for the Scorpion motor were used in the model.

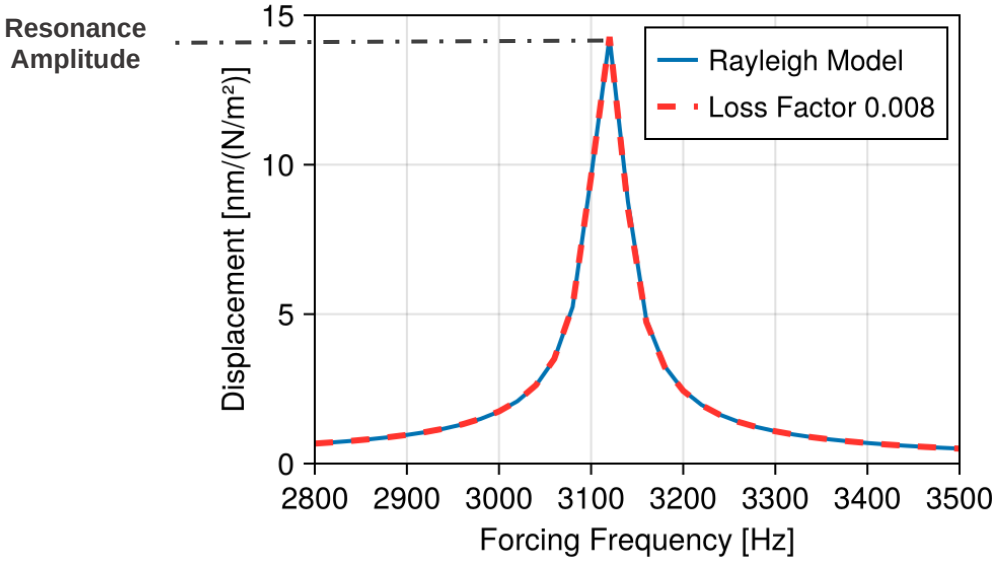


Fig. 11 Representative simulated vibration amplitude response for $m = 2$ forcing using two damping models.

The frequency response curve developed for each mode shape encapsulates all the results the mechanical vibration model is expected to predict. With several response curves, each corresponding to a different azimuthal mode shape, a given electromagnetic forcing function can be transformed into a surface vibration amplitude and mode shape suitable for the acoustic radiation model. Modeling this curve for a variety of motor geometries and mode shapes, without requiring an FEA simulation, will create a useful tool to rapidly predict rotor vibrations suitable for acoustic studies of motors within the range of geometries encompassed by the simulations.

The excellent comparison of the isotropic loss factor with the Rayleigh damping model results are expected. This simulation is performed near the Scorpion motor 3132 Hz resonance. Experimentally, the damping value at that frequency was found to be 0.003934 as shown in Table 1. In the formulation of the isotropic loss factor implemented by COMSOL Multiphysics, the loss factor is approximately twice the damping value to achieve matched results at resonance [13]. Indeed, we find excellent agreement with $0.003934 \times 2 \approx 0.008$.

A similar simulation with forcing mode $m = 4$ was performed and the results are shown in Fig. 12. The overall curve shape is similar to that for mode $m = 2$, although the width where the displacement amplitude is half the maximum value is notably larger. This increase in width indicates that the response to forcing is higher across a wider range of frequencies than the $m = 2$ case. In the $m = 2$ case the measured resonant frequency and that predicted by simulation were quite close, both near 3125 Hz. For the $m = 4$ case the simulations predict resonance near 8600 Hz while the experimentally measured $m = 4$ mode occurred at 7273 Hz. Previously, it has been observed that the accuracy of predicting the eigenfrequency decreases as the mode number and frequency increases [10].

The Rayleigh model follows the curve shown in Fig. 13 which results in increased damping values for frequencies outside of those provided by the experiments (frequencies F_1 and F_2 in Fig. 13). The Rayleigh simulation for $m = 4$, used a damping value computed at the simulation resonance frequency of roughly 8600 Hz which is higher than the

value of 7273 Hz obtained in the experiments. However, the simulation using the isotropic model used a loss factor of 0.013 computed from twice the damping value for 7273 Hz. Therefore, the isotropic simulation results in a peak displacement amplitude that is higher than that for the Rayleigh simulation as shown in Fig. 12. A new higher isotropic loss factor could be determined that creates a match between the simulations, but this value would be difficult to predict a priori and so the effort was not made here.

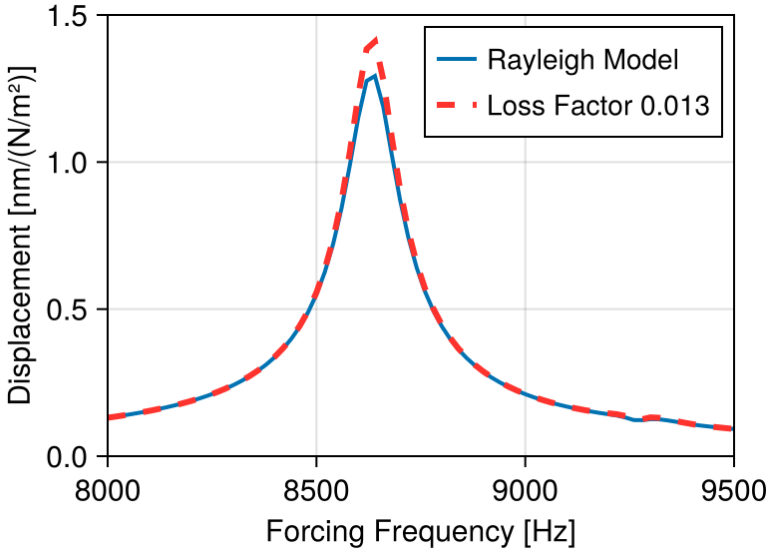


Fig. 12 Damping model comparison for *m* = 4 forcing.

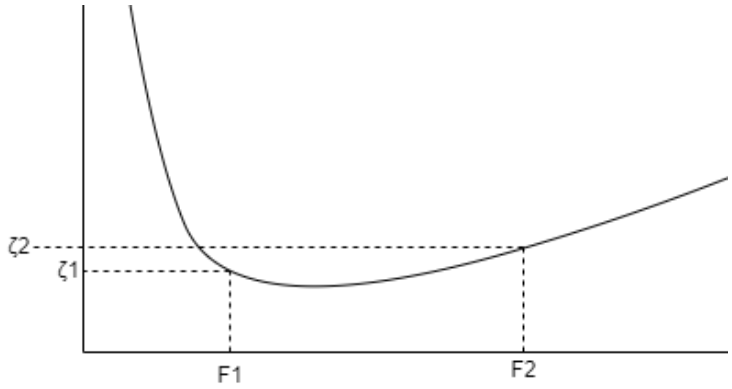


Fig. 13 Diagram of the damping value relative to user provided frequencies of the Rayleigh model.

Due to the availability of the experimental data, the remaining simulations presented herein were performed with the Rayleigh model using the damping coefficients for the Scorpion motor at 3132 Hz and 7273 Hz. While in this case the availability of experimental data provides a good basis for additional simulations, in many instances similar data may not be available. The range of experimental damping values in Table 1 is guidance for the range of isotropic loss factors that are appropriate for motors in the 1-5 kW class. The preponderance of the values lies between 0.0014 and 0.007, so as a first estimate, isotropic loss factors from 0.003 to 0.014 are reasonable.

D. Geometry Parameter Sweep

Next, we investigate the impact of different rotor geometries, first by varying the most critical dimension, the overall rotor diameter. For *m* = 2 forcing, frequency response curves for rotors with diameters ranging from 20 to 100 mm are shown in Fig. 14. The forcing frequency of each response curve has been normalized by its peak resonance frequency for that diameter. This eigenfrequency varies substantially with the diameter but the normalization aligns the peak curves as shown. The symmetry about the resonance frequency of the frequency response curve is maintained across rotors of varying diameter. The results show that increasing the rotor diameter leads to an increase in radial displacement.

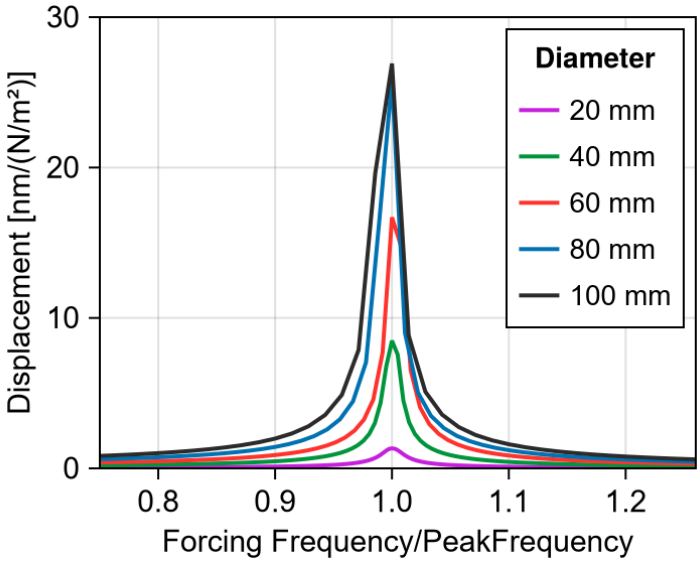


Fig. 14 Frequency response curves for aspect ratio = 2, *m* = 2 forcing, and varying outer diameter.

Similar results for variation in motor aspect ratio are shown in Fig. 15. Again, the forcing frequency has been normalized and the response curves align as a result. Here, increases in rotor aspect ratio result in decreases in rotor radial displacement.

Similar simulations can be performed for other modes. Fig. 16 shows response curves corresponding to $m = 4$ forcing for variations in diameter and aspect ratio. The overall results are similar to the $m = 2$ case, but the amplitudes are smaller for this mode. The mode $m = 4$ resonance is at a higher frequency. Damping increases with frequency causing the decreased amplitude. Another feature is the secondary peak visible in the aspect ratio = 0.7 curve of Fig. 16 (b). This secondary peak is due to a different eigenmode excited by the $m = 4$ forcing at a higher frequency than the primary resonance peak. For details on how this rotor can exhibit different eigenfrequencies excited by the same mode see Ref [10]. In the current study, this side peak can be ignored although such adjacent peaks can pose challenges to normalization and processing of large simulation parameter spaces.

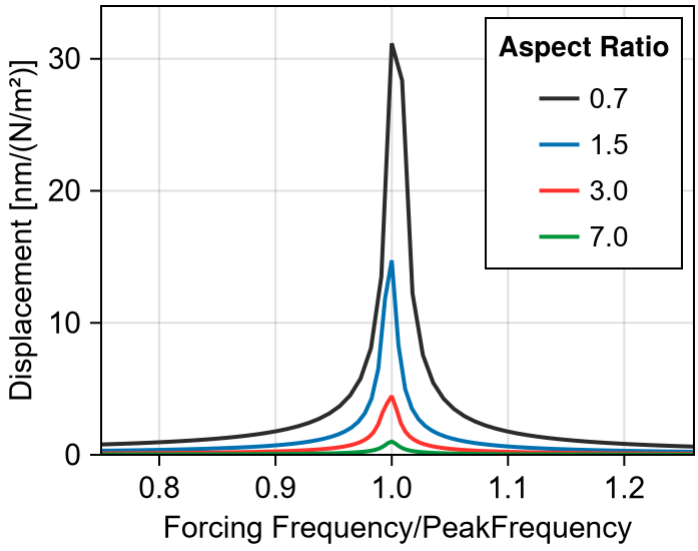


Fig. 15 Frequency response curves for diameter = 40 mm, *m* = 2 forcing, and varying aspect ratio.

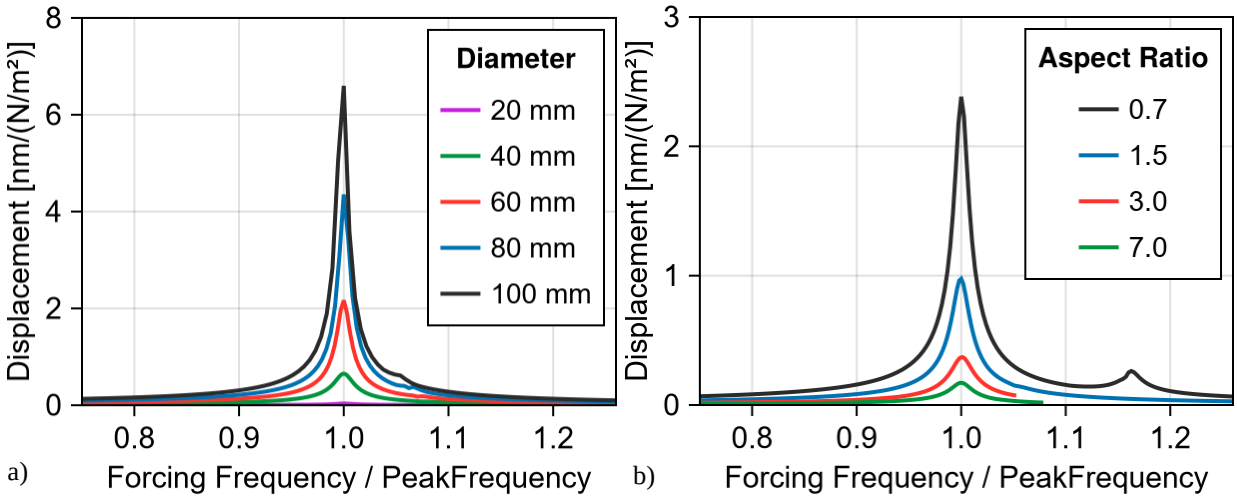


Fig. 16 Frequency response curves for *m* = 4 forcing for a) varying diameter and b) varying aspect ratio.

For both the *m* = 2 and 4 simulations and for variation in both diameter and aspect ratio, the frequency normalization has aligned each response curve, but additional normalization is required due to the discrepancies in the response curve amplitudes. If, for a particular forcing mode, the amplitude of each curve is normalized by the maximum value obtained by that curve, the response curves for the entire range of rotor geometries can be collapsed as depicted in Fig. 17. All 63 response curves generated by *m* = 2 forcing are well collapsed.

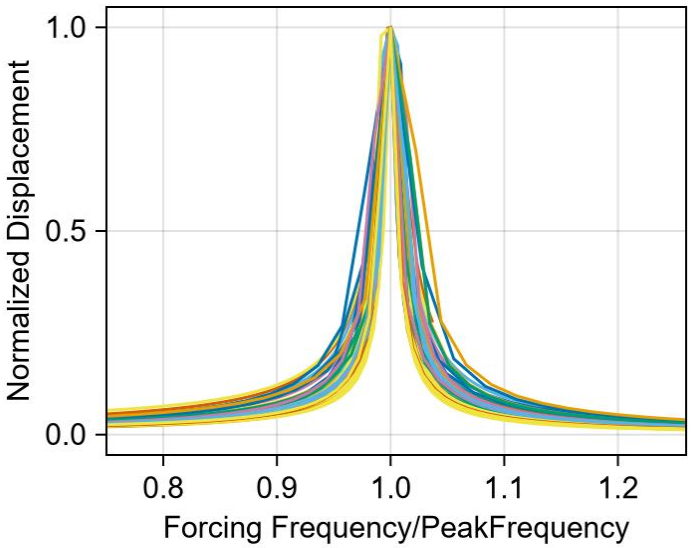


Fig. 17 Frequency response curve normalized by peak frequency and peak frequency amplitude for *m* = 2 forcing.

We are now able to fit a curve to the normalized data of Fig. 17. Given the relatively simple vibration mode shapes produced by the simulation and the close resemblance of frequency response curves, we use the traditional analytical equation that describes the motion of a simple single degree-of-freedom forced damped oscillator as the basis for a curve fit. The curve fit equation is provided in Eq. 3, where $f^* = {f}/{f_p}$ is the ratio of the forcing frequency f to the peak frequency f_p, ξ is the damping parameter of the least squares fit, and A scales the overall amplitude of the curve.

$$Normalized\ Displacement = \frac{A}{\sqrt{\left(1-f^{*2}\right)^2 + (2*\xi* f^*)^2}} \quad (3)$$

Performing a least-squares fit using Eq. 3 on the data presented in Fig. 17 results in a close curve fit as shown in Fig. 18. This indicates that the analytical damped forced oscillator solution was suitable for the simulation data. The fit coefficients are provided in Table 3.

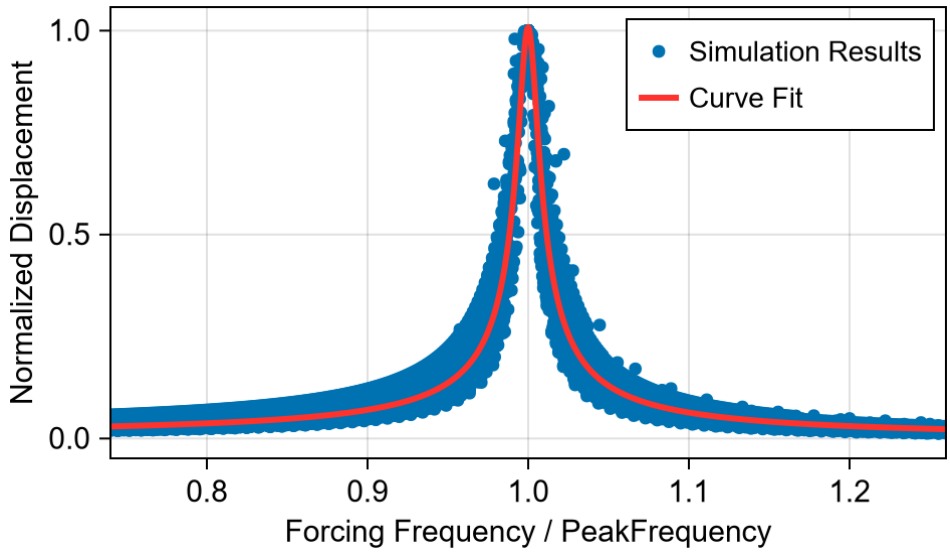


Fig. 18 Simulated frequency response curve data and curve fit for *m* = 2.

The *m* = 4 simulations can be treated similarly to the *m* = 2 simulations. Doing so produces the normalized data and curve fit in Fig. 19. The normalization of the response curves is not as good as the *m* = 2 case, but the resulting curve fit may be sufficient for a system-level tool where detailed motor design information is unavailable. The parameters of this curve fit are provided in Table 3. One consequence of the reduced normalization quality, as shown by the wider spread of the displacement results, is that the resulting curve fit does not reach 1.0 at the peak, even though, by construction, each response curve should pass through that point.

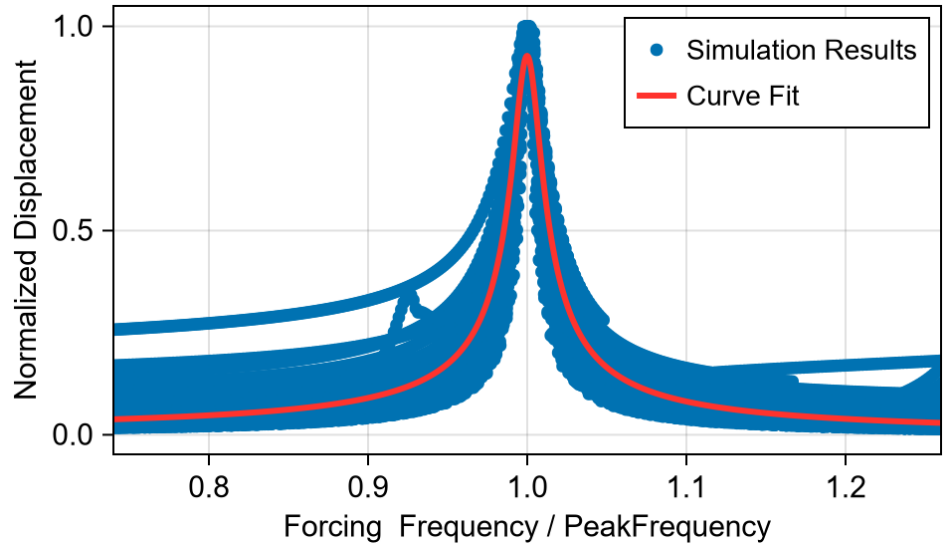


Fig. 19 Simulated frequency response curve data and curve fit for *m* = 4.

Table 3 Displacement curve fit parameters for two forcing modes.

Forcing Mode, *m*	A	ξ
2	0.0133924	0.00664659
4	0.0172172	0.00928094

Fig. 20 shows the response displacement for forcing at the resonance frequency over the range of rotor geometries for m = 2 forcing. The largest amplitudes occur at large diameters and low aspect ratios. While a two-dimensional curve fit is likely possible in this instance, a bi-linear interpolation can more directly provide peak amplitudes for a rotor geometry within this parameter space.

For m = 4 forcing, similar peak amplitude data is provided in Fig. 21. Similar trends are noted in the results for modes two and four. The amplitudes are lower for mode 4 than for mode 2. Data for both figures, suitable for interpolation, are provided in Appendix A.

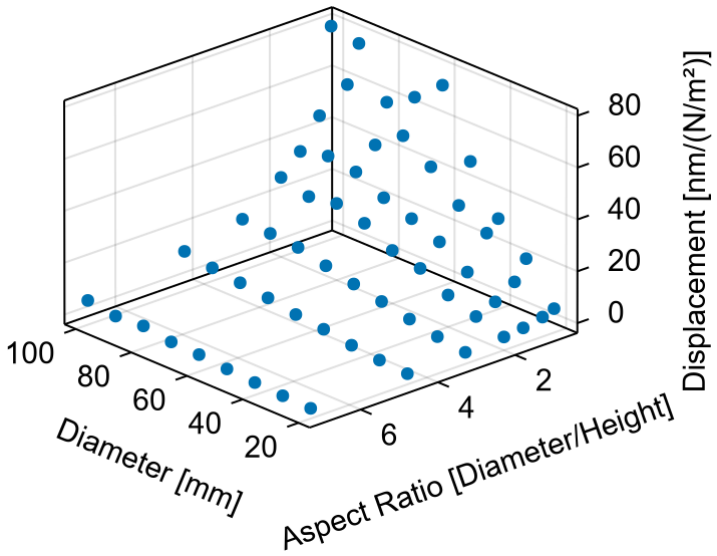


Fig. 20 Resonance displacement amplitude vs rotor geometry for *m* = 2 forcing.

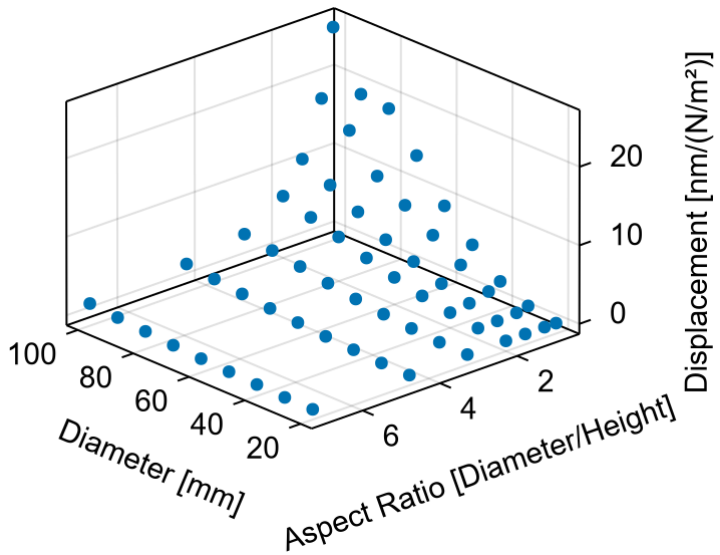


Fig. 21 Resonance displacement amplitude vs rotor geometry for *m* = 4 forcing.

To predict the surface displacement amplitude, the eigenmode and eigenfrequency are first calculated using the previously described model [10] from the electromagnetic forcing input, rotor diameter, and rotor aspect ratio. The resonance amplitude is then calculated using the corresponding mode shape data presented in Fig. 20 or Fig. 21 (and Appendix A). Using the forcing frequency ratio (f^*) and the resonance amplitude, the response amplitude normalized by the electromagnetic forcing amplitude is computed from the frequency response curves in Fig. 18 or Fig. 19. Finally, the displacement is obtained by applying the electromagnetic forcing amplitude.

IV. Conclusion

The prediction of electric-motor noise consists of three distinct elements: the determination of the electromagnetic forcing on the outer shell of the motor due to its geometry and input current; the induced structural vibrations caused by this forcing; and the resultant acoustic radiation. This work addresses the vibration element of the prediction model describing an enhancement to predict vibration amplitudes of motors in the 1-5 kW class. The other two factors are under concurrent development but are not reported on herein. The prediction is suitable for system-level design tools.

Damping values, appropriate for use in a COMSOL FEA model are experimentally determined from a set of vibration measurements. It is shown that a comparable isotropic damping value exists that may, for some motor geometries, be a usable replacement when experimental data is unavailable.

A sequence of COMSOL multi-physics finite-element analysis simulations were carried out to generate surface vibration modal responses corresponding to the parameterized model described in Ref. [10]. For the $m = 2$ azimuthal mode the normalized amplitude response closely resembles that of a first-order system. The peak amplitude of this response curve depends on the motor diameter and aspect ratio. The simulation data provides a database of these amplitudes suitable for interpolation.

Combining these components with the eigenfrequency and eigenmode model previously described, and in conjunction with an acceptable electromagnetic forcing model, a prediction of rotor surface vibrations for the acoustic component of an overall motor noise model, can be constructed. Such a model, once completed for a wider range of mode shapes and rotor geometries, could be used to guide a vehicle control law, avoiding motor operating states for which rotor resonance is particularly prevalent and circumvent potential noise issues.

Appendix A

Table 4 andTable 5 provide resonance peak data used to construct Fig. 20 and Fig. 21. These data are being provided for interpolation or curve fitting.

Table 4 $m = 2$ resonance amplitude data.

Outer Diameter [mm] \ *Aspect Ratio*	0.7	1.0	1.5	2.0	3.0	4.5	7.0
20	5.429	3.759	2.203	1.327	0.664	0.314	0.122
30	20.230	12.825	7.741	4.709	2.201	1.045	0.437
40	31.173	27.140	14.730	8.486	4.453	2.234	1.006
50	48.746	33.337	21.893	14.260	6.727	3.885	1.728
60	73.682	43.754	26.348	16.689	8.963	5.058	2.724
70	64.568	51.266	29.932	22.684	11.511	6.970	3.111
80	58.157	43.234	35.401	25.850	14.094	8.300	4.761
90	76.383	62.073	37.065	24.022	14.986	9.553	4.046
100	78.597	45.563	34.376	26.915	16.008	11.421	5.566

Table 5 *m* = 4 resonance amplitude data.

Outer Diameter [mm] \ Aspect Ratio	0.7	1.0	1.5	2.0	3.0	4.5	7.0
20	0.039	0.046	0.042	0.034	0.025	0.017	0.007
30	0.748	0.379	0.220	0.163	0.102	0.062	0.025
40	2.383	1.611	0.976	0.652	0.370	0.256	0.172
50	5.564	3.515	1.993	1.293	0.696	0.468	0.308
60	9.044	5.823	3.322	2.166	1.144	0.736	0.477
70	13.973	8.155	4.625	3.157	1.663	1.054	0.691
80	18.478	10.392	6.690	4.355	2.313	1.409	0.966
90	18.838	14.735	8.624	5.368	2.865	1.821	1.241
100	25.910	17.332	10.458	6.598	3.468	2.255	1.535

Acknowledgments

This work was sponsored by the NASA Advanced Air Vehicles Program, Revolutionary Vertical Lift Technology Project.

References

[1] Huff, D. L., and Henderson, B. S., "Electric motor noise for small quadcopters: Part 1-Acoustic Measurements," *AIAA/CEAS Aeroacoustics Conference*, 2018, pp. 2952.

[2] Henderson, B. S.,and Huff, D. L., "Electric motor noise for small quadcopters: Part II-source characteristics and predictions," *AIAA/CEAS Aeroacoustics Conference*, 2018, pp. 2953.

[3] Vijayraghavan, P., and Krishnan, R., "Noise in electric machines: A review," IEEE transactions on Industry Applications, vol. 34, no. 5, pp. 1007-1013, 1999.

[4] Gieras, J. F., Wang, C., Lai, J. C. S., and Ertugrul, N., "Analytical prediction of noise of magnetic origin produced by permanent magnet brushless motors," *IEEE International Electric Machines & Drives conference*, 2007.

[5] Gieras, J. F., Wang, C., Lai, J. C. S., *Noise of Polyphase Electric Motors*, CRC Press, 2018.

[6] Zhu, Z. Q., Howe, D., Bolte, E., and Ackermann, B., "Instantaneous magnetic field distribution in brushless permanent magnet DC motors, Part I: Open-circuit field," *IEEE transactions on magnetics*, 29.1, 1993, pp 124-135.

[7] Zhu, Z. Q., and Howe, D., "Instantaneous magnetic field distribution in brushless permanent magnet DC motors, Part II: Armature-reaction field," *IEEE transactions on magnetics*, 29.1, 1993, pp 136-142.

[8] Zhu, Z. Q., and Howe, D., "Instantaneous magnetic field distribution in brushless permanent magnet DC motors, Part III: Effect of Stator Slotting," *IEEE transactions on magnetics*, 29.1, 1993, pp 143-151.

[9] Zhu, Z. Q., and Howe, D., "Instantaneous magnetic field distribution in brushless permanent magnet DC motors, Part IV: Magnetic Field on Load," IEEE transactions on magnetics, 29.1, 1993, pp 152-158.

[10] Cluts, J. D., Henderson, B. S., and Pierson, E. L., "An Initial Electric Motor Rotor Vibration Model," *AIAA SciTech Forum*, Orlando, FL, 2024, pp. 2302.

[11] Verdyck, D., Belmans, R. J. M., "An Acoustic Model for a Permanent Magnet Machine: Modal Shapes and Magnetic Forces," *IEEE transactions on magnetics*, 29.1, 2007, pp 136-142.

[12] Cluts, J. D., Huff, D. L., Henderson, B. S., and Ruggeri, C., "Surface Vibration Measurement and Analysis for UAM/UAS Electric Motor Noise," *AIAA Aviation Forum*, 2021, pp. 2208.

[13] "Structural Mechanics Module User's Guide", COMSOL, 2022, version COMSOL 6.1, pp. 183, retrieved 16 May 2025. https://doc.comsol.com/6.1/doc/com.comsol.help.sme/StructuralMechanicsModuleUsersGuide.pdf